J. Fluid Mech. (1999), *vol.* 400, *pp.* 333–353. Printed in the United Kingdom

Three-dimensional double-diffusive convection in a porous cubic enclosure due to opposing gradients of temperature and concentration

By I. SEZAI AND A. A. MOHAMAD

Department of Mechanical Engineering, Eastern Mediterranean University, Magosa, Mersin 10, Turkey

(Received 4 January 1999 and in revised form 28 July 1999)

A three-dimensional mathematical model based on the Brinkman extended Darcy equation has been used to study double-diffusive natural convection in a fluid-saturated porous cubic enclosure subject to opposing and horizontal gradients of temperature and concentration. The flow is driven by conditions of constant temperature and concentration imposed along the two vertical sidewalls of the cubic enclosure, while the remaining walls are impermeable and adiabatic. The numerical simulations presented here span a wide range of porous thermal Rayleigh number, buoyancy ratio and Lewis number to identify the different steady-state flow patterns and bifurcations. The effect of the governing parameters on the domain of existence of the three-dimensional flow patterns is studied for opposing flows ($N < 0$). Comprehensive Nusselt and Sherwood number data are presented as functions of the governing parameters. The present results indicate that the double-diffusive flow in enclosures with opposing buoyancy forces is strictly three-dimensional for a certain range of parameters. At high Lewis numbers multiple dipole vortices form in the transverse planes near the horizontal top and bottom surfaces, which the two-dimensional models fail to detect. The dipolar vortex structures obtained are similar to those created in laboratory experiments by the injection of fluid into a stratified medium.

1. Introduction

Natural convection flow resulting from the combined action of temperature and concentration, which is also called double-diffusive convection, has recently been the subject of intense research activity in view of its importance in various engineering and geophysical problems. Among these are the migration of moisture through the air contained in fibrous insulations and grain storage installations, solute exchange in sediments in coastal environments, the transport of chemical contaminants through water-saturated soil and disposal of nuclear wastes in underground sites. As reviewed by Song & Viskanta (1994) the mushy zone existing during the solidification of alloys consists of a fine mesh of dendritic crystals growing into the melt, owing to the solubility difference between the solid and liquid phases. The composition of the resulting solid is generally different from that of the melt when a melt of two or more components solidifies. Therefore, heat and mass transfer occur simultaneously in the mushy zone, which can be modelled as double-diffusive convection in a porous medium.

Heat and solute diffuse at different rates, as a result of which complex flow structures may form which have no counterpart in buoyant flows driven by a single component. Research in this field is mainly based on two configurations. The first

situation is concerned with a fluid-saturated horizontal porous layer subjected to vertical temperature and concentration gradients (Taunton, Lightfoot & Green 1972; Taslim & Narusawa 1986; Trevisan & Bejan 1987; Murray & Chen 1989; Rosenberg & Spera 1992; Chen & Chen 1993). The studies on horizontal porous layers were primarily directed to the establishment of a criterion for the onset of motion via stationary and oscillatory modes, on the basis of a linear stability analysis.

The second configuration involves vertical porous enclosures subjected to horizontal temperature and concentration gradients either by imposing uniform heat and mass fluxes or constant temperature and concentration on the vertical boundaries. In this category some of the studies are concerned with cooperating double-diffusion where the flow is driven in the same direction by the thermal and solutal forces (Trevisan & Bejan 1986; Alavyoon 1993; Mamou *et al.* 1995*b*; Goyeau, Songbe & Gobin 1996). The case of double-diffusive convection in a vertical enclosure due to opposing buoyancy forces has also been investigated. Trevisan & Bejan (1985) studied double-diffusive convection in a square porous cavity for both aiding ($N > 0$) and opposing ($N < 0$) buoyancy forces due to horizontal gradients of temperature and concentration in the range $-5 \leqslant N \leqslant +3$, where N is the solutal to thermal buoyancy ratio. The two-dimensional numerical results based on the Darcy model were compared with that of a scaling analysis. Alavyoon, Masuda & Kimura (1994) extended the analytical boundary layer solution developed earlier for aiding flow in a porous cavity subject to constant gradients of temperature and concentration at the vertical walls (Alavyoon 1993) to include the opposing buoyancy forces. In addition, the phenomenon of oscillating convection in vertical porous cavities, subject to opposing horizontal gradients of temperature and concentration, has also been investigated. The existence of multiple solutions for double-diffusive flow in a vertical enclosure subject to opposing fluxes of heat and solute was demonstrated analytically and numerically by Mamou, Vasseur & Bilgen (1995*a*). The effects of non-Darcy flow parameters such as Darcy number and porosity on heat and mass transfer within a rectangular enclosure subject to both aiding and opposing gradients of heat and mass has been investigated by Nithiarasu, Seetharamu & Sundararajan (1996) using a generalized porous medium approach. Recently, Mamou, Vasseur & Bilgen (1998) studied the onset of double-diffusive natural convection in an inclined porous cavity with equal and opposing buoyancy forces due to the imposition of transverse gradients of temperature and concentration. The critical stability limit was investigated through a numerical linear stability analysis using the Galerkin finite element method.

However, all of the above-mentioned studies are limited by the assumption of two-dimensional flow and nothing can be inferred about the possible development of three-dimensional flow patterns. To the best of our knowledge, three-dimensional analysis of double-diffusive natural convection in fluid-saturated porous enclosures subject to horizontal opposing gradients of temperature and concentration has not been reported prior to the present work. In the present study the existence of three-dimensional flow patterns in a fluid-saturated porous cubic cavity subject to opposing horizontal temperature and concentration gradients is demonstrated using a three-dimensional non-Darcy model. The effect of the governing parameters on the domain of existence of the three-dimensional flow patterns is studied and the influence of the main parameters on the average Sherwood and Nusselt numbers is investigated.

For certain parameter ranges it has been found that the flow structure is three-dimensional with secondary flow formation in the transverse plane, which the two-dimensional models fail to capture. Specially, for opposing flows at high Lewis numbers, local density anomalies occur near the top and bottom walls, with alternating

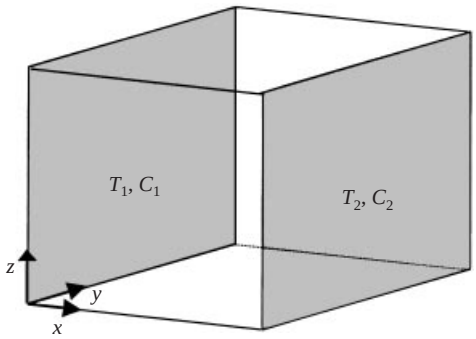

FIGURE 1. Physical model and the coordinate system.

high- and low-concentration regions. As a result dipolar vortices are found to exist, similar to those formed by the injection of fluid into a stratified medium in the laboratory experiments of Fuentes & Heijst (1994) and Flor & Heijst (1994).

2. Problem formulation

The geometry under consideration is a porous cubic cavity, saturated with a binary fluid such as an aqueous solution (figure 1). Different temperatures and concentrations are specified between the left-hand (T_1, C_1) and right-hand vertical walls (T_2, C_2), where $C_1 > C_2$ and $T_1 > T_2$, and zero heat and mass fluxes are imposed on the remaining walls. The flow is assumed to be laminar and steady. The binary fluid is assumed to be Newtonian, incompressible and to satisfy the Boussinesq approximation. The porous medium is assumed to be isotropic, homogeneous and in thermodynamic equilibrium with the fluid. Finally, the Soret and Dufour effects are assumed to be negligible. The fluid density is assumed to be constant, except in the driving term of the Navier–Stokes equations, where it varies linearly with the local temperature and solute mass fraction as

$$\rho = \rho_0[1 - \beta_T(T - T_0) - \beta_C(C - C_0)], \tag{1}$$

where

$$\beta_T = -\frac{1}{\rho}\left[\frac{\partial \rho}{\partial T}\right]_C \quad \text{and} \quad \beta_C = -\frac{1}{\rho}\left[\frac{\partial \rho}{\partial C}\right]_T, \tag{2}$$

with $\beta_T > 0$ and $\beta_c < 0$. The thermophysical properties of the fluid are taken as constant and they are estimated at a reference temperature T_0 and solute mass fraction C_0, which are set to be equal to T_2 and C_2, respectively. Using the following dimensionless variables: $X = x/L$, $Y = y/L$, $Z = z/L$, $\boldsymbol{V} = \boldsymbol{v}L/\nu$, $P = pL^2/\rho\nu^2$, $\Theta = (T - T_2)/(T_1 - T_2)$, $\Phi = (C - C_2)/(C_1 - C_2)$ where L is the length of one side of the cubic cavity and ν is the kinematic viscosity of the fluid, the equations governing the conservation of mass, momentum, energy and species concentration in non-dimensional form can be written as (Goyeau *et al.* 1996)

$$\nabla \cdot \boldsymbol{V} = 0, \tag{3}$$

$$\frac{1}{\varepsilon^2}(\boldsymbol{V} \cdot \nabla)\boldsymbol{V} = -\nabla P + \frac{Ra_T}{Pr}(\Theta + N\Phi)\boldsymbol{k} - \frac{1}{Da}\boldsymbol{V} + \Lambda\nabla^2\boldsymbol{V}, \tag{4}$$

$$\boldsymbol{V} \cdot \nabla\Theta = \frac{1}{Pr}\lambda\nabla^2\Theta \tag{5}$$

$$\boldsymbol{V}\cdot\nabla\Phi=\frac{1}{Le\,Pr}\nabla^2\Phi, \tag{6}$$

where $Ra_T=(g\beta_T\Delta TL^3)/v\alpha$ is the thermal Rayleigh number, $N=Ra_S/Ra_T$ the ratio of the buoyancy forces, $Ra_S=(g\beta_C\Delta CL^3)/v\alpha$ the solutal Rayleigh number, $Da=K/L^2$ the Darcy number, $Pr=v/\alpha$ the Prandtl number, $Le=\alpha/D$ the Lewis number and $\alpha=k/\rho_0C_p$ is the effective thermal diffusivity. The parameters g, $\boldsymbol{k}$, C_p, D and k refer to gravitational acceleration, unit vector in vertical direction, specific heat, molecular diffusivity of the fluid and effective thermal conductivity, respectively. A positive value of N results in augmenting convection (cooperative buoyancy forces) and a negative value leads to opposing flow.

Equation (4) represents the Brinkman extended Darcy model where the Forchheimer inertia term is dropped as suggested by Lauriat & Prasad (1987) due to the fact that for all computations in this study the particle Reynolds number defined by

$$Re=\frac{\rho vK^{0.5}}{\mu} \tag{7}$$

is less than unity. K and ε are the permeability and porosity of the porous medium. $\Lambda=\mu'/\mu$ is the ratio of the effective viscosity in the Brinkman term to fluid viscosity. The variation in Λ is not fully understood and most of the works on non-Darcy formulation consider $\Lambda=1$. Finally, $\lambda=k_m/k_f$ is the ratio of thermal conductivities of the porous medium and the fluid. The average heat and mass fluxes at the left-hand wall are given in non-dimensional terms by Nusselt and Sherwood numbers as

$$Nu=\int_0^1\int_0^1\left[\frac{\partial\Theta}{\partial X}\right]_{x=0}\mathrm{d}Y\,\mathrm{d}Z\quad\text{and}\quad Sh=\int_0^1\int_0^1\left[\frac{\partial\Phi}{\partial X}\right]_{x=0}\mathrm{d}Y\,\mathrm{d}Z. \tag{8}$$

3. Numerical method

Equations (3)–(6) are discretized using staggered non-uniform control volumes. In order to minimize the numerical diffusion errors, the QUICK scheme (Leonard 1979) is used in approximating the advection terms. The flux limiter known as ULTRA-SHARP (Leonard & Mokhtari 1990) is used to eliminate the non-physical oscillations inherent in the QUICK scheme. To alleviate the convergence problems the method is implemented in the solution procedure using the deferred correction approach suggested by Khosla & Rubin (1974). The SIMPLEC algorithm (Van Doormaal & Raithby 1984) is used to couple the momentum and continuity equations. The momentum equations are solved by applying one iteration of the strongly implicit procedure (SIP) of Stone (1968) which is extended here to handle three-dimensional problems. The pressure correction equation is solved iteratively by applying the conjugate gradient (CG) method (Hackbush 1994) until the sum of absolute residuals has fallen by a factor of ten. The coefficient matrix resulting from the discretization of the energy and species concentration equations is non-symmetric and solved iteratively by the Bi-CGSTAB method (Van der Vorst 1992). SSOR preconditioning (Hackbush 1994) is used for accelerating the convergence rates of both CG and Bi-CGSTAB methods. Generally, under-relaxation factors of 0.7, 0.7, 0.7, 1.0, 0.9 and 0.9 were applied to U, V, W, P, T and C, respectively. For a few cases only, under-relaxation factors for T and C had to be reduced to 0.5 where convergence problems were met.

To avoid the excessively high computer times inherent in the solution of three-dimensional natural convection problems, a full approximation storage (FAS) full multigrid (FMG) method (Hortmann, Peric & Scheuerer 1990) is used to solve

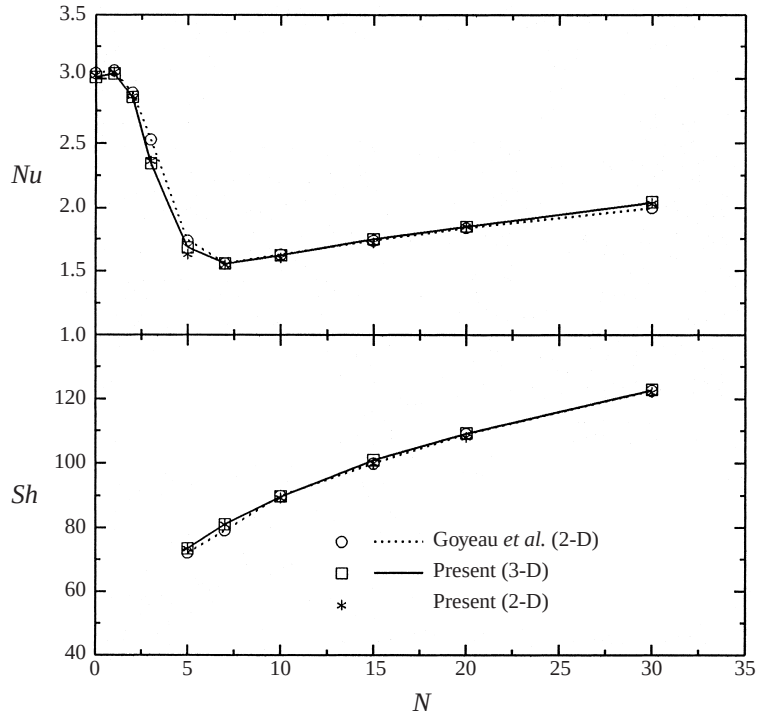

FIGURE 2. Comparison with the two-dimensional results of Goyeau *et al.* (1996). $Ra^* = 100$, $Le = 100$, $Da = 10^{-5}$, $Pr = 10$.

the problem, which removes a wider spectrum of wavelengths more efficiently than single grid methods. The equations are solved by a four-level fixed V-cycle procedure starting at the coarsest grid and progressing to the finest grid level. For prolongation operations tri-linear interpolation is used for all variables. For restriction, the area-weighted average procedure is used for all quantities defined on the control-volume surface such as velocities. The volume-weighted average procedure is adopted for all quantities defined at the control-volume centre such as pressure, temperature and concentration. $80 \times 80 \times 80$ grids are used on the finest level with denser grid clustering near boundaries using the sine function for the grid distribution.

To ensure convergence of the numerical algorithm the following criterion is applied to all dependent variables over the solution domain

$$\frac{\sum |\phi_{ijk}^m - \phi_{ijk}^{m-1}|}{\sum |\phi_{ijk}^m|} \leqslant 10^{-5}, \tag{9}$$

where ϕ represents a dependent variable U, V, W, P, T and C, the indexes i, j, k indicate a grid point and the index m the current iteration at the finest grid level.

In the steady-state approach adopted, the lack of convergence of the solution may be interpreted as an indication of time-dependent states for the range of parameters investigated. The CPU time required for convergence was approximately from 1 to 4 h on a 300 MHz Pentium II personal computer with 256 MB RAM, using single-precision arithmetic with a Fortran 90 compiler.

Due to the absence of three-dimensional numerical data, the validation of the three-dimensional code has been performed by comparison with the two-dimensional

extended Brinkman formulation of Goyeau *et al.* (1996). As will be shown later, there is a marked difference between the two- and three-dimensional model results for opposing buoyancies for certain parameter ranges, where the flow regime is three-dimensional. For this reason the comparison is done for positive values of N, where the flow structure is found to be two-dimensional. The comparison of the average Nusselt and Sherwood numbers is shown in figure 2 for the sinusoidal distribution of an $80 \times 80 \times 80$ mesh system. The results of the two-dimensional version of our code are also included in the figure. It can be seen that for the rather high Lewis number of 100, both versions of our code perform well over the range $0 < N < 30$, for values of the porous thermal Rayleigh number $Ra^* = Ra_T\ Da = 100$ and $Da = 10^{-5}$.

4. Results and discussion

The numerical model is used to investigate the domain of steady three-dimensional flow patterns and the resulting heat and mass transfer characteristics of double-diffusive convection in a porous cubic enclosure subject to opposing solutal and thermal buoyancy forces ($N < 0$). The value of N is varied between -0.1 and -10 and Le is varied between 1.0 and 1000, for $Ra^* = 1.0$–500. The other parameters are kept constant: the Prandtl number of the fluid ($Pr = 10$), as well as the porous-medium properties ($\Lambda = 1$, $\lambda = 1$, $\varepsilon = 1$, $Da = 10^{-5}$).

The range of parameters used are typical of the mushy zone in solidification experiments using ammonium chloride (NH_4Cl) (Nishimura & Imoto 1994) or Na_2CO_3 solutions (Bénard *et al.* 1996), which are widely considered to be good analogues for metallic alloys, such as lead–tin, aluminium–copper and nickel–aluminium, as discussed by Huppert (1990). The NH_4Cl or Na_2CO_3 solutions are much easier to handle than their metallic counterparts since the liquid phase is transparent. A typical range of Prandtl number values for these solutions is 10 to 13. Bénard *et al.* (1996) give the range of Lewis numbers during their experiments with Na_2CO_3 as $186 < Le < 194$.

Quantitative measurement of mushy-layer properties is difficult because the forest of dendrites makes the region opaque and assessment of porosity–permeability relationships is still a difficulty in modelling such regions. However, in practice the Darcy number is known to be roughly proportional to the square of the dentrite spacing and is typically 10^{-3} or smaller (Schulze & Worster 1998).

4.1. *Flow structures*

Due to the thermal and solutal boundary conditions considered here, the left-hand sidewall has a higher temperature and higher concentration than the right-hand sidewall. As a result, the direction of the flow due to thermal buoyancy forces is clockwise, whereas the direction of the flow due to solutal buoyancy depends on the sign of the concentration expansion coefficient β_C. The direction of solutal flow is counterclockwise for β_C or $N < 0$, opposing the thermal flow, which is the case considered in this study.

In figures 3 and 4 the effects of the buoyancy ratio are illustrated for $Ra^* = 100$ and $Le = 10$. For $-0.3 \leqslant N \leqslant 0$ the flow pattern is two-dimensional, where the fluid is observed to flow in the (X, Z)-plane with no secondary flow formation on the transverse planes. Figure 3 shows the results obtained for $N = -0.5$. The flow is driven by the thermal buoyancy force, so that the main flow direction is clockwise in the (X, Z)-plane. The resulting flow pattern, isotherms and iso-concentration lines on different planes clearly show that the flow is no longer parallel to the (X, Z)-plane. The projection of streamlines on the mid (X, Z)-plane are not closed, but

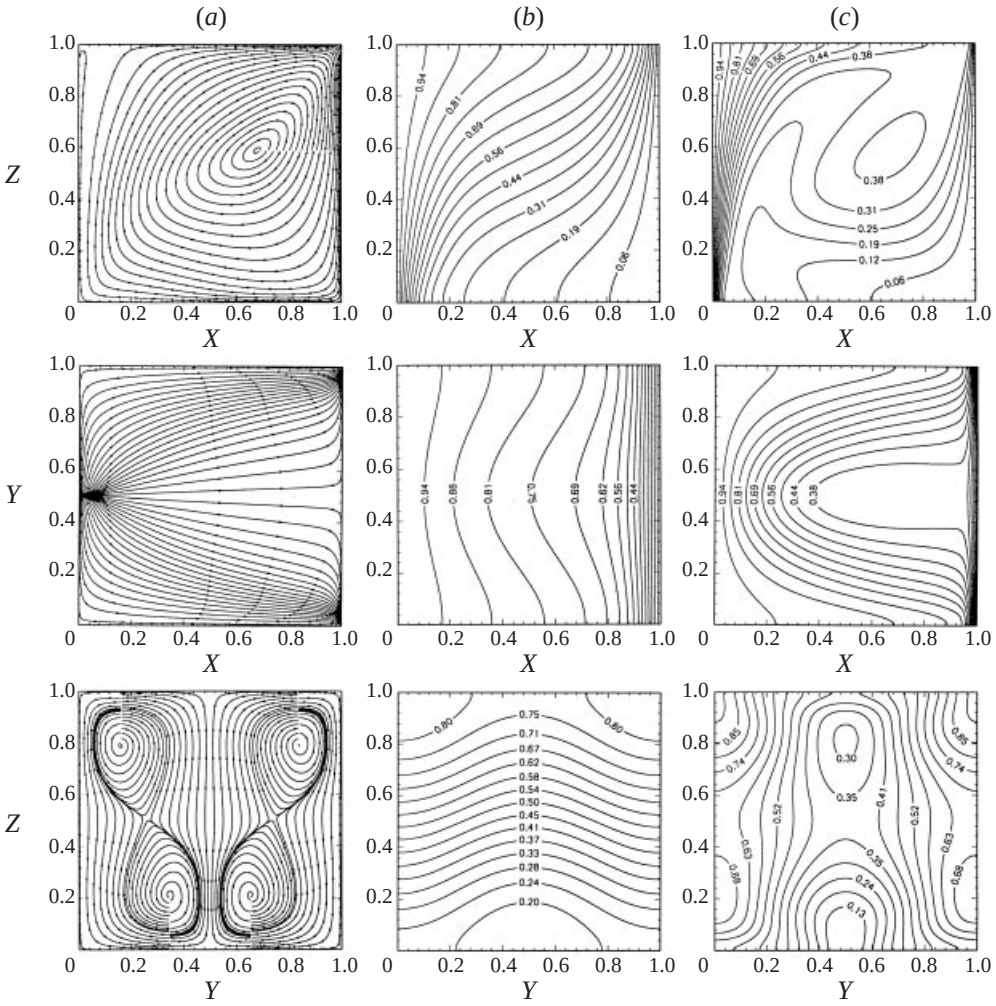

FIGURE 3. Projection of (*a*) streamlines, (*b*) isotherms and (*c*) concentration lines on the mid (X, Z)-plane (top), (X, Y)-plane at $Z = 0.9$ (middle) and mid (Y, Z)-plane (bottom), for $Ra^* = 100$, $Le = 10$ and $N = -0.5$.

have a spiral form. The spiralling of the streamlines implies that the gradient of the out-of-plane velocity component $(\partial V/\partial Y)$ is non-zero which is an indication of the three-dimensionality of the flow field. This can be observed from the projection of streamlines onto the (X, Y)-plane at $Z = 0.9$ where the streamlines are no longer parallel to the x-axis but diverge towards the sidewalls. The three-dimensional nature of the flow field is shown more clearly on the streamline plots on the mid (Y, Z)-plane $(X = 0.5)$, where the flow consists of two oppositely rotating secondary flow cells, each containing two smaller vortices, all superimposed on the main flow on the (X, Z)-plane. It is demonstrated by the concentration contours on the mid (Y, Z)-plane that low-concentration fluid is advected to the roof of the cavity at $Y = 0.5$ as a result of buoyancy forces. Upon hitting the top wall it separates into two branches towards the sidewalls, where the concentration is maximum. As a result, the high-density fluid descends along the lateral walls. However, due to the sharp negative concentration gradient the density decreases away from the lateral walls where a buoyant flow is

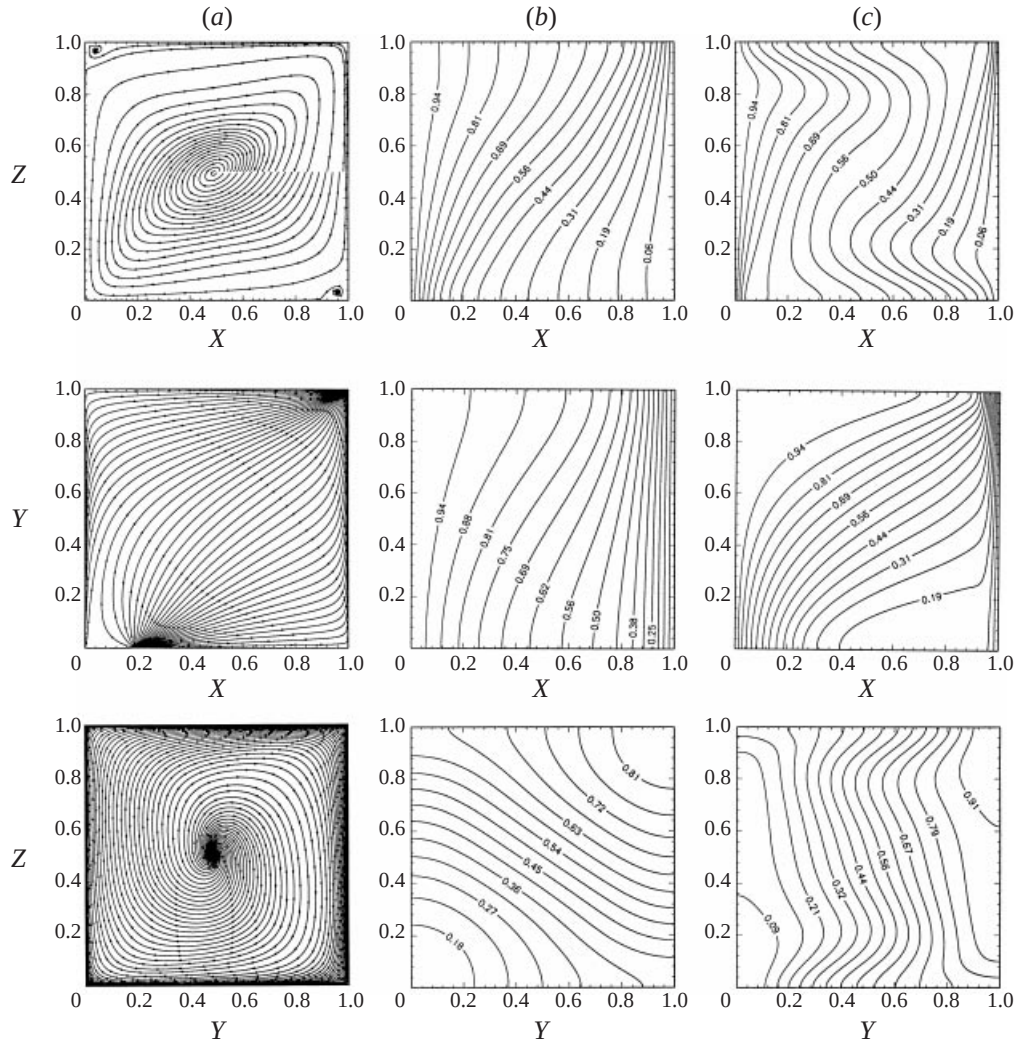

FIGURE 4. As figure 3 but at $N = -0.7$.

set up in the core of the cavity, which opposes the descending flow, thus leading to vortex formation in the upper half of the cavity.

The flow field in the mid (X, Z)-plane shown in figure 3 exhibits a non-symmetric profile with respect to the $X = 0.5$ and $Z = 0.5$ axes, which is contrary to the known steady two-dimensional results for double-diffusive flow in both porous and non-porous square cavities. Previous two-dimensional studies on double-diffusive convection in square cavities, whether porous or not, indicate centro-symmetric rotating flow structures in the steady state. In their two-dimensional study on double-diffusive convection with equal and opposing buoyancy forces in a non-porous cavity, Ghorayeb, Khallouf & Mojtabi (1999) point out that convective steady-state flow is centro-symmetric regardless of *Le* and that it is asymmetric only in the oscillatory mode for some Lewis number values. The loss of symmetry in the three-dimensional double-diffusive steady flow patterns in the mid (X, Z)-plane shown in figures 3 and 7 is in contrast to previous two-dimensional studies and needs further investigation.

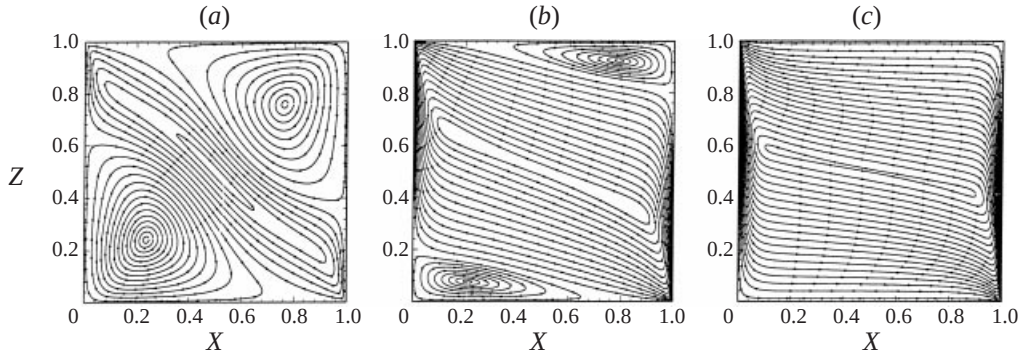

FIGURE 5. Multi-cell flow patterns in the two-dimensional flow regime for $Ra^* = 100$ and $Le = 10$. (*a*) $N = -1.0$, (*b*) $N = -2.0$, (*c*) $N = -5.0$.

Upon decreasing N to -0.7 the opposing mass species buoyancy starts to exert more influence and the system bifurcates to a different mode. The determination of the exact value of N for this transition is not attempted in this study. The resulting flow, isotherm and concentration patterns are presented in figure 4. The projection of streamlines on the mid (X, Z)-plane have a spiral form with two smaller eddies near the top-left and bottom-right corners. In this case the three-dimensional flow is characterized by a secondary spiral motion on the (Y, Z)-plane, superimposed on the main flow rotation on the (X, Z)-plane. The rotation sense of the spiral roll on the (Y, Z)-plane is believed to depend on the initial disturbances caused by numerical noise. The resultant flow proceeds along the diagonal as observed from the flow patterns on the (X, Y)-plane at $Z = 0.9$.

For $N = -0.8$ and -0.9 no steady convergent solution could be obtained. Residuals of velocities oscillate continuously, which may be an indication of a time-dependent flow field in this range. Alavyoon *et al.* (1994) found that oscillating motion exists in cases where the contribution of the gradients of temperature and concentration to buoyancy are of comparable magnitude. For $N \leqslant -1.0$ the resultant steady-state flow patterns are two-dimensional, with no secondary flows in the (Y, Z)- or (X, Y)-planes. In this range the flow patterns, isotherms and mass concentration profiles are found to be similar to the two-dimensional results of Mamou *et al.* (1995*a*). Figure 5 illustrates the projection of streamlines on the mid (X, Z)-plane. For $N = -1$ the flow consists of a solutally driven counterclockwise rotating cell in the central part of the cavity and two thermally driven clockwise circulations adjacent to the cavity corners. The multi-cell pattern is lost for $N < -2$, where the thermally driven cells disappear and the whole flow is primarily driven by the solutal buoyancy.

To assess the effect of the porous medium, simulations have also been done for double-diffusive convection in the cubic enclosure without any porous medium, for wide range of flow parameters. Somewhat similar three-dimensional flow structures were obtained with secondary flow formation in the (Y, Z)-planes (Sezai & Mohamad 1999). Thus, it seems that the three-dimensional nature of the flow structure is the result of double-diffusive convection but not due to the presence of the porous medium.

If the Lewis number is increased to 100 the flow becomes three-dimensional for N as low as -0.2. Figure 6 illustrates the projection of streamlines, isotherms and iso-concentration lines on different planes for $N = -0.2$, $Le = 100$ and $Ra^* = 100$. A rather complex flow pattern results with secondary flow vortices on the mid (Y, Z)-

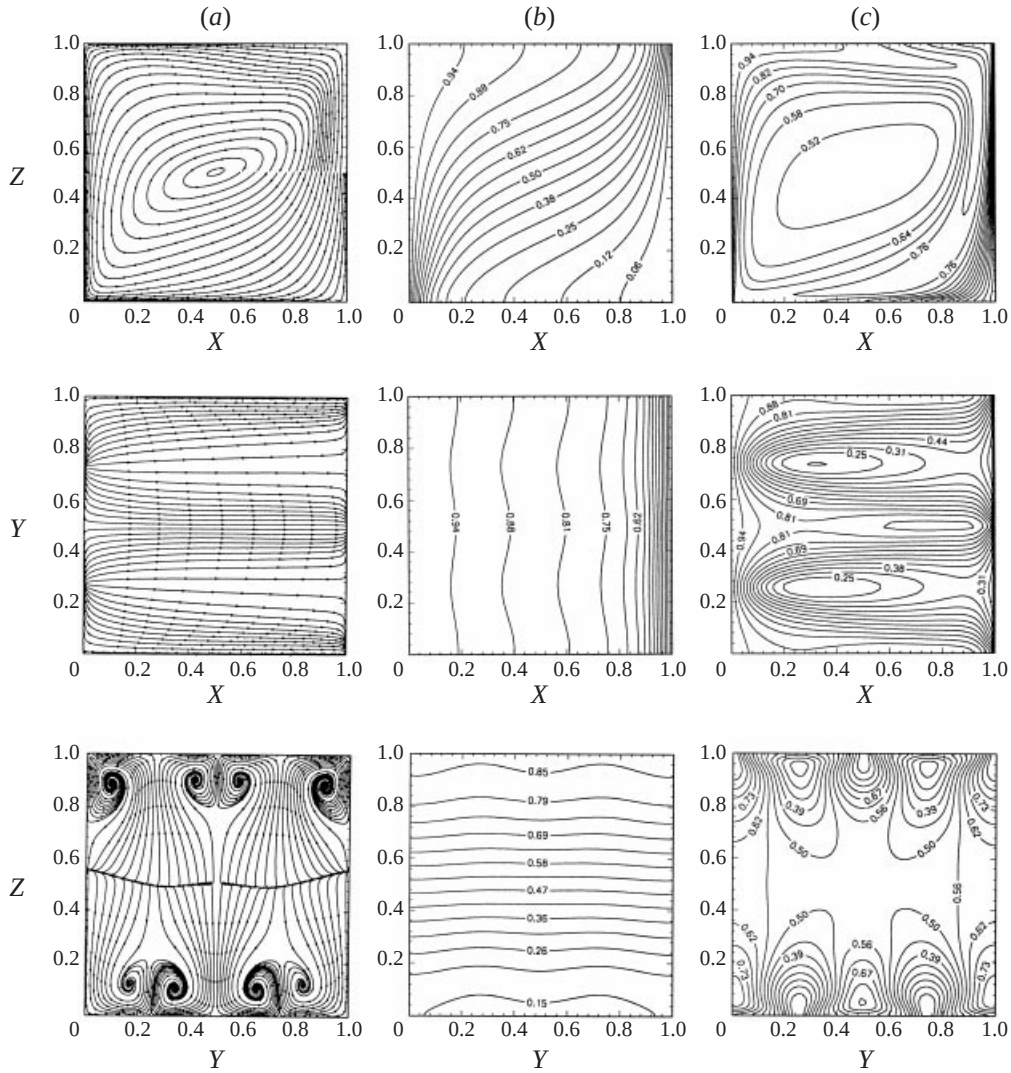

FIGURE 6. Projection of (*a*) streamlines, (*b*) isotherms and (*c*) concentration lines on the mid (X, Z)-plane (top), (X, Y)-plane at $Z = 0.9$ (middle) and mid (Y, Z)-plane (bottom), for $Ra^* = 100$, $Le = 100$ and $N = -0.2$.

plane near the top and bottom walls due to the increasing effect of the opposing mass species buoyancy forces. The corresponding iso-concentration plots on the mid (Y, Z)-plane and (X, Y)-plane at $Z = 0.9$ indicate alternating high- and low-concentration regions. The iso-concentration plot on the mid (Y, Z)-plane indicates low-concentration regions near the top and bottom walls at $Y \approx 0.25$ and $Y \approx 0.75$. The rising fluid in these low-concentration regions separates into two branches upon hitting the top wall, as observed from the flow patterns on the mid (Y, Z)-plane, and flows towards higher concentration regions, where it gets heavier and descends downward. The descending flow is opposed by the buoyant flow where two dipolar vortices form at the top half of the cavity consisting of two counter-rotating vortices. For the fluid descending at the lower half of the cavity at $Y \approx 0.25$ and $Y \approx 0.75$, the concentration decreases as it approaches the bottom wall thereby creating an

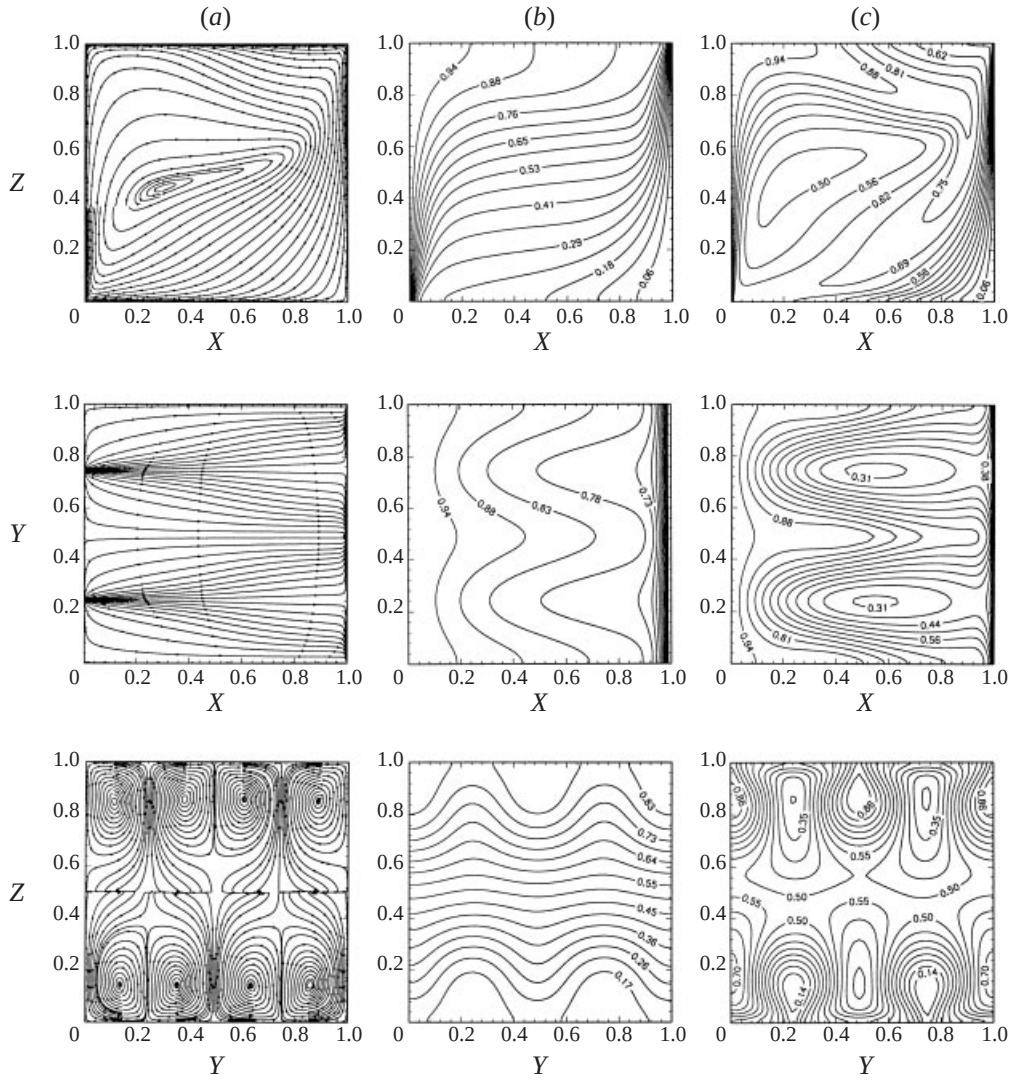

FIGURE 7. Projection of (*a*) streamlines, (*b*) isotherms and (*c*) concentration lines on the mid (X, Z)-plane (top), (X, Y)-plane at $Z = 0.9$ (middle) and mid (Y, Z)-plane (bottom), for $Ra^* = 500$, $Le = 10$ and $N = -0.4$.

opposing buoyant flow. As a result the positions of the two dipolar vortices formed near the bottom wall are displaced by an amount equal to the distance between the minimum and maximum concentration points near the horizontal walls.

For $Ra^* = 500$ and $Le = 10$ the flow structure is three-dimensional for $N \leqslant -0.3$ (for N increasing in the negative direction). Examples of the resulting flow structure, isotherms and iso-concentration lines are given in figure 7 for $N = -0.4$.

Again four pairs of dipolar vortices are formed on the mid (Y, Z)-plane, which expand to fill the whole domain. The dipolar vortex structure in the top half of the cavity is similar to the vortex dipoles created by horizontal injection of fluid into a stratified medium in laboratory experiments (Flor & Heijst 1994; Fuentes & Heijst 1994). The dipolar vortex consists of two closely packed patches of oppositely

signed vorticity and has a two-dimensional character. The dipolar vortices are known to provide an efficient mechanism for the transport of mass and momentum and are believed to play an important role in the transport of scalar properties such as salt and heat in oceans (Fuentes & Heijst 1994). Again, the alternating high- and low-concentration regions near the top and bottom walls are evident from the iso-concentration lines at the mid (Y, Z)-plane and (X, Y)-plane at $Z = 0.9$, as a result of which the isotherms are highly distorted.

However, it seems that the mechanisms that lead to the formation of the dipolar vortices in this study are different from those created by the injection of fluid into a stratified medium. In the present study the dipolar vortex structure appears to be the result of the interaction of the fluid flow with the horizontal walls of the cavity and is accompanied by the formation of alternating low- and high-concentration regions in the porous medium at high Lewis numbers. Dipolar vortices form when falling high-concentration or rising low-concentration fluid parcels are opposed by the main fluid flow. However, no such dipolar vortices could be found from simulation results obtained in a non-porous cubic cavity.

For $Ra^* = 500$ and $Le = 100$ the flow structure becomes three-dimensional for N as low as -0.1. The resulting flow structure, isotherms and iso-concentration plots on different planes are shown in figure 8. In this case the number of dipolar vortices increased to six, with corresponding low- and high-concentration regions. For larger negative N-values the flow becomes time dependent as judged from the oscillating mass residuals where no convergent steady solution could be obtained.

4.2. *Heat and mass transfer*

4.2.1. *Effect of buoyancy ratio*

The effect of buoyancy ratio N on the average Nusselt and Sherwood numbers is depicted in figures 9(a) and 9(b), respectively, for $Ra^* = 10$ and $Le = 10$. The variation of the secondary flow structure on the mid (Y, Z)-plane is illustrated in figure 10. Starting from pure heat transfer results at $N = 0$ both the Nusselt and Sherwood numbers decrease upon increasing the magnitude of N in the negative direction. This is due to the fact that the flow driven by the thermal buoyancy effect is weakened more by the opposing buoyancy effect due to solutal variations as N becomes more negative. As the thermal and solutal buoyancy forces approach being equal but opposite in direction, the net body forces on the rising fluid near the heated wall diminish, as it approaches the turning point near the top of the cavity, where the concentration is highest. This can be observed from the concentration profile in the mid (X, Z)-plane, shown earlier in figure 3. As a result, fluid movement in the lateral direction becomes possible, since an additional degree of freedom is available for the fluid to flow in the lateral direction in the cubic cavity, as shown in the flow profile on the horizontal (X, Y)-plane at $Z = 0.9$ in figure 3. The heavier fluid descends the lateral walls, setting up a secondary flow in the (Y, Z)-plane where the flow becomes three-dimensional. The steady three-dimensional character of the flow is retained for $-0.8 < N < -0.3$. Outside this range, where either the thermal or solutal buoyancy forces dominate, the three-dimensional effects are suppressed, the flow is confined to the (X, Z)-plane and the flow structure becomes two-dimensional. The flow bifurcates to an oscillatory mode for $-0.92 < N < -0.8$.

The above results are for zero initial velocity, temperature and concentration fields. If the results for $N = -0.7$ are used as initial conditions and N is varied in steps, then the upper branch of the solutions shown in figures 9(a) and 9(b) is obtained. On this branch of solutions the spiral-type flow pattern in the mid (Y, Z)-plane is retained

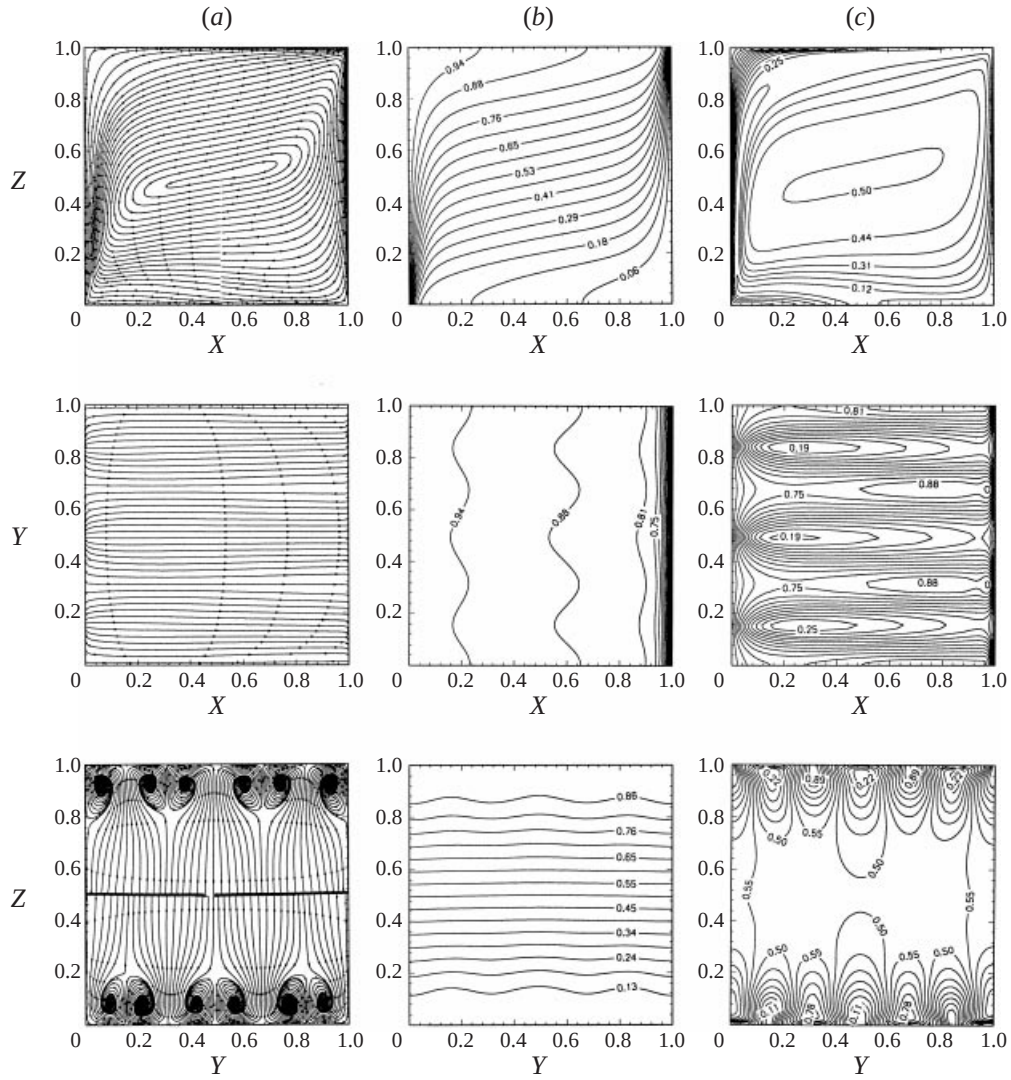

FIGURE 8. Projection of (*a*) streamlines, (*b*) isotherms and (*c*) concentration lines on the mid (X, Z)-plane (top), (X, Y)-plane at $Z = 0.9$ (middle) and mid (Y, Z)-plane (bottom), for $Ra^* = 500$, $Le = 100$ and $N = -0.1$.

between $N = -0.45$ and -0.8. However, the effect of these multiple solutions on the average Nusselt and Sherwood numbers is quite small and barely noticeable on the scale given in figure 9.

Simulations have also been done using a two-dimensional model with the same grid distribution as that of the three-dimensional model and the results are compared in figure 9. Both the Nusselt and Sherwood numbers are in close agreement for values of N where the flow is two-dimensional. This is expected, as the retarding effect of the lateral sidewalls is negligible due to the low flow velocities inherent in porous media. However, in the range where the flow structure is three-dimensional, there is a marked difference between the two- and three-dimensional model results for both Nusselt and Sherwood numbers. The difference increases as the effects of the opposing buoyancy

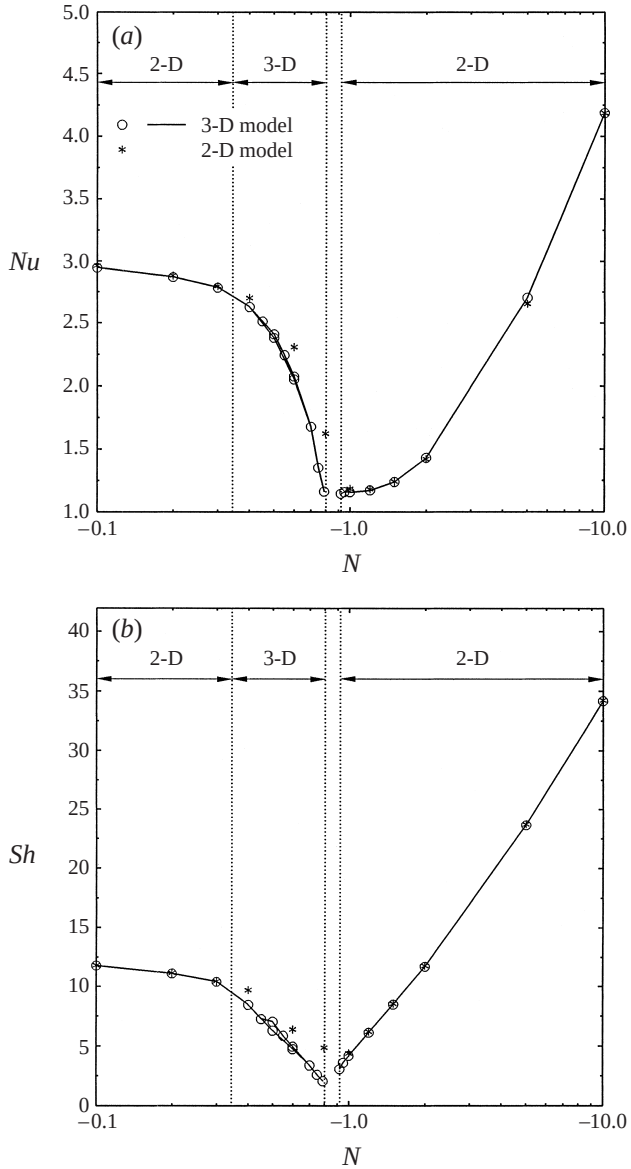

FIGURE 9. (*a*) Nusselt number and (*b*) Sherwood number, vs. the buoyancy ratio ($Ra^* = 100$, $Le = 10$).

forces approach being equal in magnitude, reflecting the effect of three-dimensional flow structure, with secondary flow in the (Y, Z)-plane superimposed on the main flow rotation.

For $N \approx -1.0$ both Nu and Sh are minimum and close to the diffusive solution, where the buoyancy forces induced by the thermal and solutal effects are opposing and of equal intensity. As the magnitude of N is increased beyond -1.0 both Nu and Sh increase due to increasing of the opposing effect of the solutal buoyancy where the flow becomes increasingly more solutally dominated.

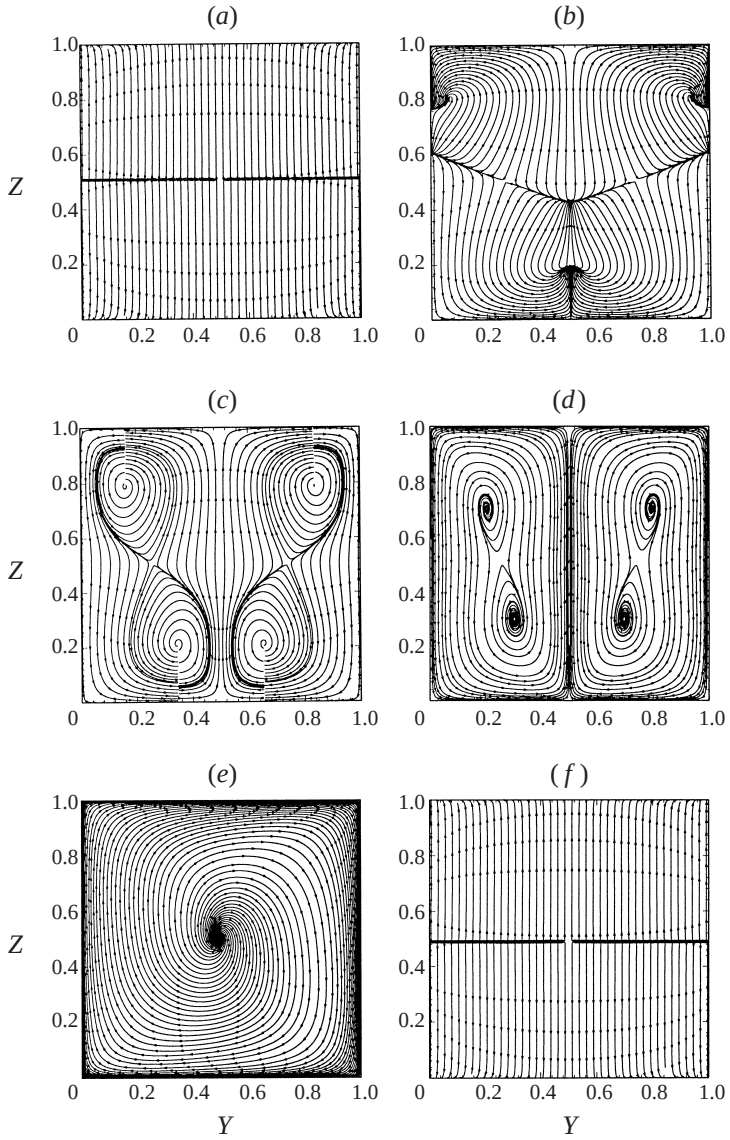

FIGURE 10. The secondary flow patterns on the mid (Y, Z)-plane for different buoyancy ratios: (*a*) $N = -0.3$, (*b*) $N = -0.4$, (*c*) $N = -0.5$, (*d*) $N = -0.6$, (*e*) $N = -0.7$, (*f*) $N = -1.0$ ($Ra^* = 100$, $Le = 10$).

4.2.2. *Effect of Lewis Number*

The effect of the Lewis number on the average Nusselt and Sherwood numbers for opposing flows in the transition region is illustrated in figure 11 for $N = -0.5$ and $Ra^* = 10$. The variations of the secondary flow structures on the mid (Y, Z)-plane as the Lewis number increases are illustrated in figure 12 for zero initial velocity, temperature and concentration fields. For $Le \leqslant 20$ the flow structure is two-dimensional with no secondary flows on the (Y, Z)- or (X, Y)-planes. For these low Lewis numbers the flow field is essentially controlled by the concentration field. For $Le \approx 22$, bifurcation from two- to three-dimensional structure takes place, where

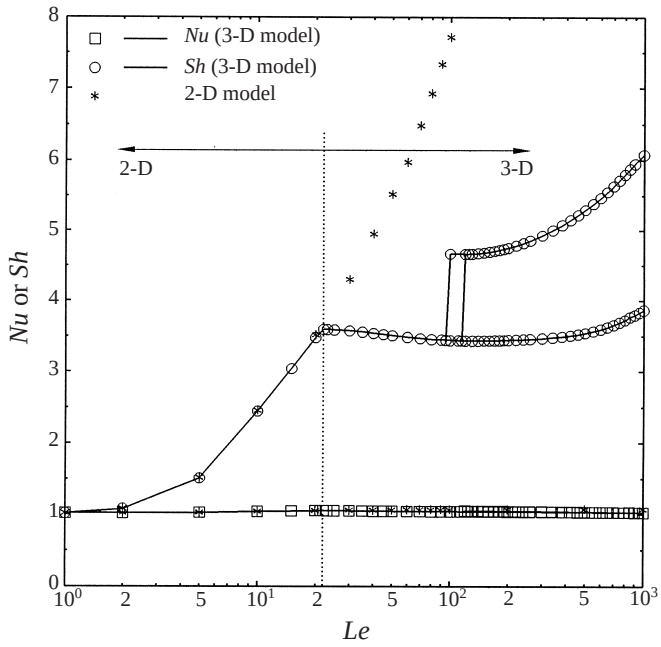

FIGURE 11. Nusselt and Sherwood numbers vs. Lewis number ($N = -0.5$, $Ra^* = 10$).

a rotational flow is also set up in the (Y, Z)-plane, which is superimposed on the main flow rotation in the (X, Z)-plane. It is well known that all nonlinear dynamic systems have some universal features; when some controlling parameter (Le, Ra, N, etc.) is varied then the system undergoes a series of bifurcations that ultimately lead to chaos. The formation of secondary flows on the transverse planes marks the transition of the flow structure prior to the first bifurcation. For $23 < Le < 90$ the secondary flow structure on the mid (Y, Z)-plane consists of a single spiral roll superimposed on the main flow rotation in the (X, Z)-plane. In this range the Sherwood number decreases slightly with Lewis number. On the other hand if zero velocity, temperature and concentration fields are used as initial conditions then the system undergoes a bifurcation to another mode at a Lewis number between 95 and 100, the exact determination of which is not attempted in this study. This is accompanied by a sudden rise in the rate of mass transfer, where the upper solution branch in figure 11 is followed. The resulting flow structure consists of two counter-rotating secondary flow cells in the (Y, Z)-plane superimposed on the main roll cell in the (X, Z)-plane. The Sherwood number again increases with Lewis number for $Le > 90$. For these large Lewis numbers the velocity field is now primarily controlled by the thermal buoyancy. The Nusselt number is close to unity for all Lewis numbers at this rather low porous thermal Rayleigh number, indicating a conduction-dominated heat transfer.

Starting from the solution obtained for $Le = 10^3$ on the upper branch and decreasing the Lewis number gradually after a convergent solution is obtained for a given Le, it is found that the bifurcation from the upper to the lower branch takes place at a Lewis number between 115 and 120. On the other hand, starting from $Le = 1.0$ and repeating the above procedure with increasing Lewis numbers results in the lower branch of the solutions.

The results obtained from the two-dimensional model are also shown in figure 11, and they are observed to be almost the same as those of the three-dimensional model

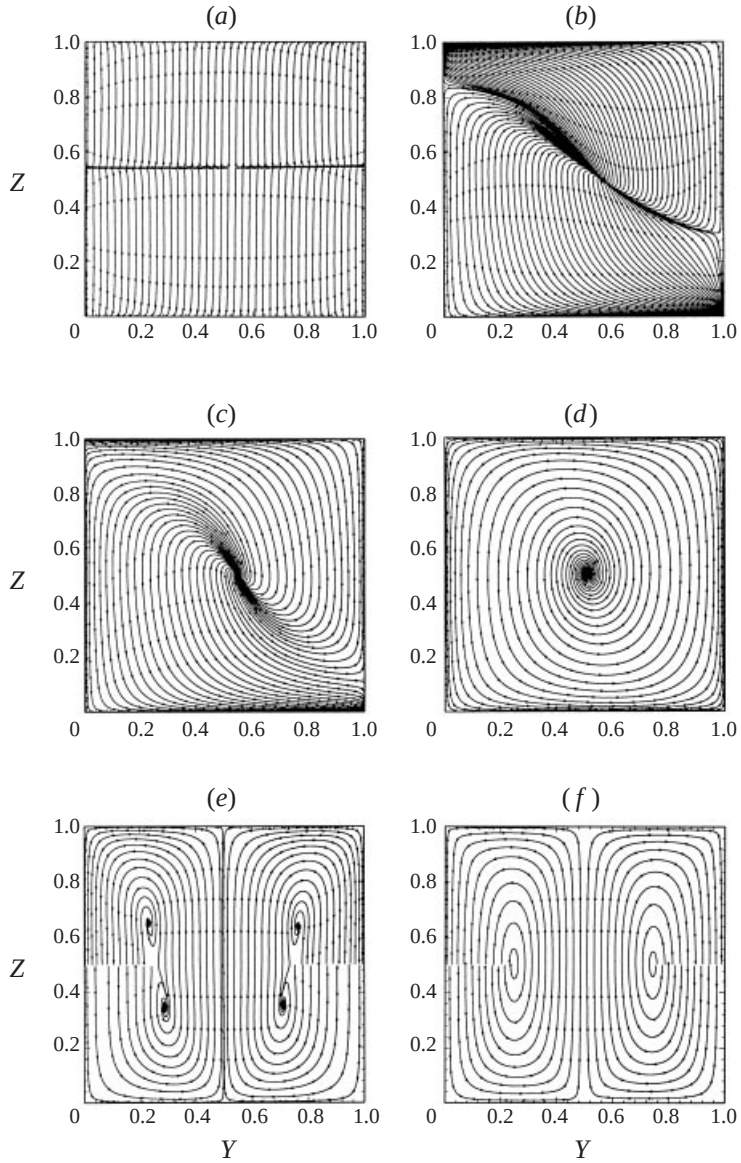

FIGURE 12. The secondary flow patterns on the mid (Y, Z)-plane for different Lewis numbers: (*a*) $Le = 20$, (*b*) $Le = 22$, (*c*) $Le = 23$, (*d*) $Le = 90$, (*e*) $Le = 100$, (*f*) $Le = 1000$ ($Ra^* = 10$, $N = -0.5$).

up to a Lewis number where transition to three-dimensional flow structure starts. At this point the two-dimensional solution follows a completely different branch, yielding much higher Sh values.

4.2.3. *Effect of porous thermal Rayleigh number*

Figure 13 gives an example of the influence of the porous thermal Rayleigh number on the Nusselt and Sherwood numbers for $N = -0.5$ and $Le = 10$. Figure 14 illustrates the evolution of the corresponding flow patterns on the mid (Y, Z)-plane as the porous thermal Rayleigh number increases with zero initial velocity, temperature

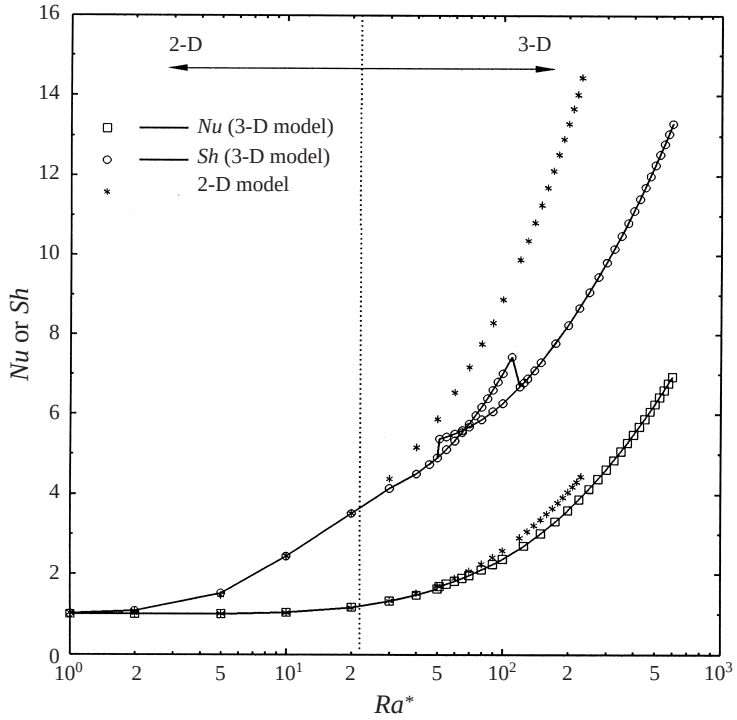

FIGURE 13. Nusselt and Sherwood numbers vs. porous thermal Rayleigh number ($N = -0.5$, $Le = 10$).

and concentration fields. When Ra^* is small enough ($Ra^* < 30$) the flow pattern is controlled by concentration and the resulting flow structure is two-dimensional. However, for $Ra^* \approx 30$ in addition to the main flow rotation on the (X, Z)-plane a secondary flow starts in the (Y, Z)-plane, where transition to three-dimensional flow structure takes place. For $Ra^* \approx 51$ the system bifurcates to a totally different structure accompanied by a sudden jump in the Sherwood number (figure 13), for zero initial velocity, temperature and concentration fields. Four counter-rotating secondary flow vortices appear on the (Y, Z)-plane, the sizes of which increase with porous thermal Rayleigh number. When Ra^* increases to about 400 each of these vortices splits into two, resulting in a rather complicated flow structure dominated by the thermal buoyancy forces.

The same solution branch is obtained by decreasing the porous thermal Rayleigh number gradually after each convergent solution, where the Sherwood number drops suddenly at $Ra^* \approx 51$. However, repeating the above procedure with increasing Ra^* results in a smooth increase of Sherwood number up to $Ra^* \approx 115$–120, where a bifurcation to a new state takes place with a sudden fall in Sh. No convergent steady solution could be obtained for $Ra^* > 600$, which may be due to oscillatory flow.

The results obtained from the two-dimensional model agree very closely with those of the three-dimensional model in the range where the flow structure is two-dimensional (figure 13). However, in the three-dimensional region, the two-dimensional model over-predicts both the Nusselt and Sherwood numbers due to its failure to detect the effects of the secondary flow in the transverse plane.

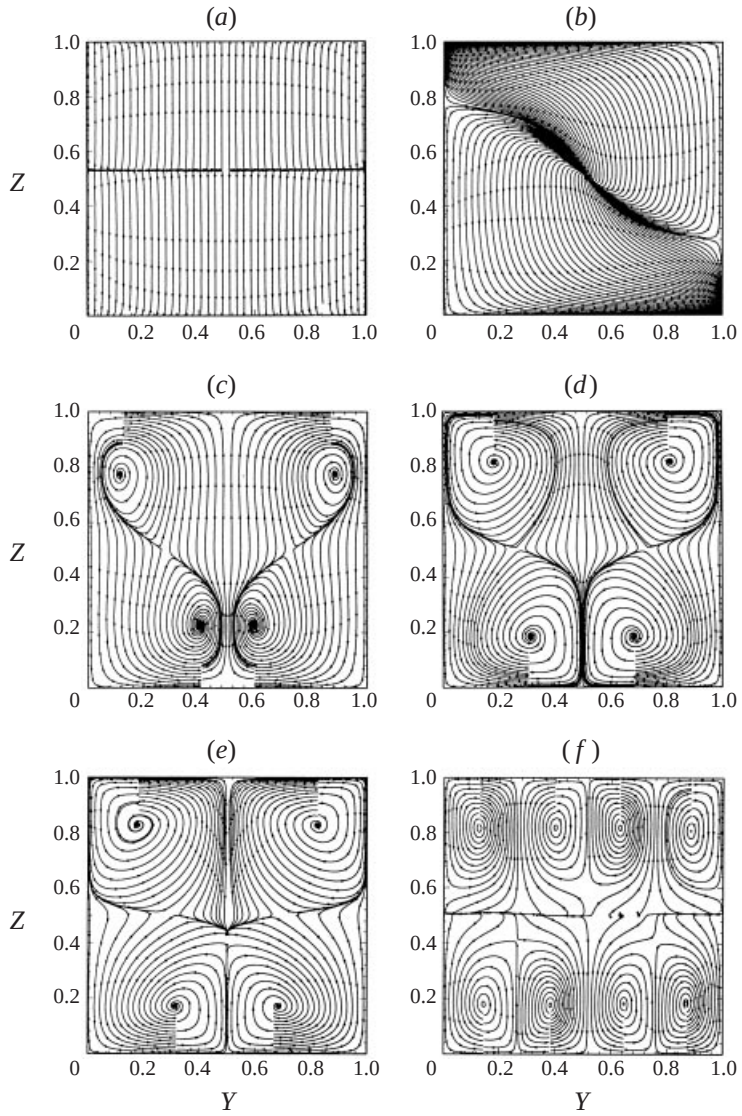

FIGURE 14. The secondary flow patterns on the mid (Y, Z)-plane for different thermal Rayleigh–Darcy numbers: (*a*) $Ra^* = 20$, (*b*) $Ra^* = 50$, (*c*) $Ra^* = 60$, (*d*) $Ra^* = 200$, (*e*) $Ra^* = 300$, (*f*) $Ra^* = 400$ ($Le = 10$, $N = -0.5$).

5. Conclusion

The present work is an attempt to model the three-dimensional aspects of thermosolutal natural convection in a porous cubic enclosure subject to horizontal and opposing gradients of temperature and concentration. The main controlling parameters, such as porous thermal Rayleigh number, Lewis number and buoyancy ratio are varied to gain new insights into the formation of different flow patterns. The main findings of the present investigation can be summarized as follows:

(1) Upon increasing N from zero in the negative direction there is a critical value of the buoyancy ratio where secondary flow is set up in the transverse plane, superimposed on the main flow rotation, which cannot be detected by two-dimensional

models. As N is increased further the concentration buoyancy forces become approximately equal and opposite to the thermal buoyancy forces, where the flow becomes oscillatory. For larger negative N-values solutal buoyancy forces dominate, where a reversal to the two-dimensional flow structure occurs.

(2) For given values of N and Ra^* the effect of the Lewis number was investigated. For relatively low Lewis numbers, where the flow is dominated by solutal buoyancy, the resulting flow structure is two-dimensional. In this range Sh increases with Le, while Nu is close to unity, indicating a diffusive heat transfer mechanism. For higher Lewis numbers the magnitude of the thermal buoyancy forces increases and at a critical value of Le the flow structure becomes three-dimensional, characterized by a secondary spiral-type rotation, in addition to the main flow rotation. In this range Sh decreases slightly. As the Lewis number is increased further the system bifurcates to a completely different three-dimensional steady state.

(3) A similar behaviour is observed when the porous thermal Rayleigh number is changed at fixed N and Le. Following the two-dimensional flow structure at relatively small Ra^* a transition state is reached where the flow becomes three-dimensional. Several flow bifurcations are detected at higher Ra^* values, where the flow is characterized by complex three-dimensional pattens.

REFERENCES

Alavyoon, F. 1993 On natural convection in vertical porous enclosures due to prescribed fluxes of heat and mass at the vertical boundaries. *Intl J. Heat Mass Transfer* **36**, 2479–2498.

Alavyoon, F., Masuda, Y. & Kimura, S. 1994 On natural convection in vertical porous enclosures due to opposing fluxes of heat and mass prescribed at the vertical walls. *Intl J. Heat Mass Transfer* **37**, 195–206.

Bénard, C., Bénard, R., Bennacer, R. & Gobin, D. 1996 Melting driven thermohaline convection. *Phys. Fluids* **8**, 112–130.

Chen, F. & Chen, C. F. 1993 Double-diffusive fingering convection in a porous medium. *Intl J. Heat Mass Transfer* **36**, 793–807.

Flor, J. B. & Heijst, G. J. F. van 1994 An experimental study of dipolar vortex structures in a stratified fluid. *J. Fluid Mech.* **279**, 101–133.

Fuentes, O. U. V. & Heijst, G. J. F. van 1994 Experimental study of dipolar vortices on a topographic β-plane. *J. Fluid Mech.* **239**, 79–106.

Ghorayeb, K., Khallouf, H. & Mojtabi, A. 1999 Onset of oscillatory flow in double-diffusive convection. *Intl J. Heat Mass Transfer* **42**, 629–643.

Goyeau, B., Songbe, J. P. & Gobin, D. 1996 Numerical study of double-diffusive natural convection in a porous cavity using the Darcy Brinkman formulation. *Intl J. Heat Mass Transfer* **39**, 1363–1378.

Hackbush, W. 1994 *Iterative Solution of Large Sparse Systems of Equations*. Springer.

Hortmann, M., Peric, M. & Scheuerer, G. 1990 Finite volume multigrid prediction of laminar natural convection: bench-mark solutions. *Intl J. Numer. Meth. Fluids* **11**, 189–207.

Huppert, H. E. 1990 The fluid mechanics of solidification. *J. Fluid Mech.* **212**, 209–240.

Khosla, P. K. & Rubin, S. G. 1974 A diagonally dominant second-order accurate implicit scheme. *Comput. Fluids* **2**, 207–209.

Lauriat, G. & Prasad, V. 1987 Natural convection in a porous cavity: a numerical study for Brinkman extended Darcy formulation. *J. Heat Transfer*, **109**, 688–696.

Leonard, B. P. 1979 A stable and accurate convective modeling procedure based on quadratic upstream interpolation. *Comput. Meth. Appl. Mech. Engng* **19**, 59–98.

Leonard, B. P. & Mokhtari, S. 1990 Beyond first order upwinding: the ULTRA-SHARP alternative for nonoscillatory steady-state simulation of convection. *Intl J. Numer. Meth. Engng* **30**, 729–766.

Mamou, M., Vasseur, P. & Bilgen, E. 1995*a* Multiple solutions for double-diffusive convection in a vertical porous enclosure. *Intl J. Heat Mass Transfer* **38**, 1787–1798.

Mamou, M., Vasseur, P. & Bilgen, E. 1998 A Galerkin finite element study of the onset of double-diffusive convection in an inclined porous enclosure. *Intl J. Heat Mass Transfer* **41**, 1513–1529.

Mamou, M., Vasseur, P., Bilgen, E. & Gobin, D. 1995*b* Double-diffusive convection in an inclined slot filled with porous medium. *Eur. J. Mech.* B **14**, 629–652.

Murray, B. T. & Chen, C. F. 1989 Double-diffusive convection in a porous medium. *J. Fluid Mech.* **201**, 147–166.

Nishimura, T. & Imoto, T. 1994 Occurrence and development of double-diffusive convection during solidification of a binary system. *Intl J. Heat Mass Transfer* **37**, 1455–1464.

Nithiarasu, P., Seetharamu, K. N. & Sundararajan, T. 1996 Double-diffusive natural convection in an enclosure filled with fluid-saturated porous medium: a generalized non-Darcy approach. *Numer. Heat Transfer* A **30**, 413–426.

Rosenberg, N. D. & Spera, F. J. 1992 Thermohaline convection in a porous medium heated from below. *Intl J. Heat Mass Transfer* **35**, 1261–1273.

Schulze, T. P. & Worster, M. G. 1998 A numerical investigation of steady convection in mushy layers during the directional solidification of binary alloys. *J. Fluid Mech.* **356**, 199–220.

Sezai, I. & Mohamad, A. A. 1999 Double diffusive convection in a cubic enclosure with opposing temperature and concentration gradients. *Phys. Fluids* (submitted).

Song, M. & Viskanta, R. 1994 Natural convection flow and heat transfer within a rectangular enclosure containing a vertical porous layer. *Intl J. Heat Mass Transfer* **37**, 2425–2438.

Stone, H. L. 1968 Iterative solution of implicit approximations of multi-dimensional partial differential equations. *SIAM J. Numer. Anal.* **5**, 530–558.

Taslim, M. & Narusawa, U. 1986 Binary fluid composition and double-diffusive convection in a porous medium. *J. Heat Transfer* **108**, 221–224.

Taunton, J., Lightfoot, E. & Green, T. 1972 Thermohaline instability and salt fingers in a porous medium. *Phys. Fluids* **15**, 748–753.

Trevisan, O. V. & Bejan, A. 1986 Mass and heat transfer by natural convection in a vertical slot filled with porous medium. *Intl J. Heat Mass Transfer* **29**, 403–415.

Trevisan, O. V. & Bejan, A. 1987 Mass and heat transfer by high Rayleigh number convection in a porous medium heated from below. *Intl J. Heat Mass Transfer* **30**, 2341–2356.

Van der Vorst, H. A. 1992 BiCGSTAB: A fast and smoothly converging variant of Bi-CG for the solution of non-symmetric linear systems. *SIAM J. Sci. Statist. Comput.* **13**, 631–644.

Van Doormaal, J. P. & Raithby, G. D. 1984 Enhancements of the simple method for predicting incompressible fluid flows. *Numer. Heat Transfer* **7**, 147–163.